LANGMUIR Article
Cite This: Langmuir 2019, 35, 15651−15660
pubs.acs.org/Langmuir

Electrochemically Enhanced Dissolution of Silica and Alumina in Alkaline Environments

Howard A. Dobbs,[†,¶] George D. Degen,[†,¶] Zachariah J. Berkson,[†,●] Kai Kristiansen,[†] Alex M. Schrader,[†] Tandré Oey,[§] Gaurav Sant,[§,∥,⊥] Bradley F. Chmelka,[†,*] and Jacob N. Israelachvili[†,‡]

[†]Department of Chemical Engineering and [‡]Materials Department, University of California, Santa Barbara, California 93106, United States

[§]Department of Civil and Environmental Engineering, [∥]Department of Materials Science and Engineering, and [⊥]California Nanosystems Institute, University of California, Los Angeles, California 90095, United States

Supporting Information

ABSTRACT: Dissolution of mineral surfaces at asymmetric solid−liquid−solid interfaces in aqueous solutions occurs in technologically relevant processes, such as chemical/mechanical polishing (CMP) for semiconductor fabrication, formation and corrosion of structural materials, and crystallization of materials relevant to heterogeneous catalysis or drug delivery. In some such processes, materials at confined interfaces exhibit dissolution rates that are orders of magnitude larger than dissolution rates of isolated surfaces. Here, the dissolution of silica and alumina in close proximity to a charged gold surface or mica in alkaline solutions of pH 10−11 is shown to depend on the difference in electrostatic potentials of the surfaces, as determined from measurements conducted using a custom-built electrochemical pressure cell and a surface forces apparatus (SFA). The enhanced dissolution is proposed to result from overlap of the electrostatic double layers between the dissimilar charged surfaces at small intersurface separation distances (<1 Debye length). A semiquantitative model shows that overlap of the electric double layers can change the magnitude and direction of the electric field at the surface with the less negative potential, which results in an increase in the rate of dissolution of that surface. When the surface electrochemical properties were changed, the dissolution rates of silica and alumina were increased by up to 2 orders of magnitude over the dissolution rates of isolated compositionally similar surfaces under otherwise identical conditions. The results provide new insights on dissolution processes that occur at solid−liquid−solid interfaces and yield design criteria for controlling dissolution through electrochemical modification, with relevance to diverse technologies.

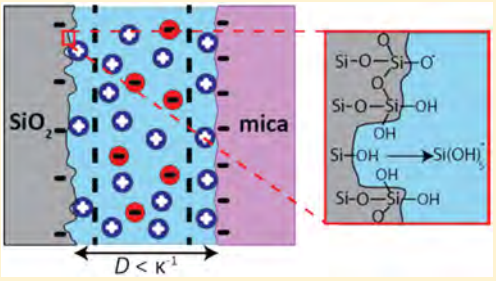

INTRODUCTION

Dissolution of inorganic materials in aqueous environments influences the development of macroscopic properties in many natural and technological systems. For example, partial dissolution and condensation of aluminosilicate particles in dense, highly alkaline slurries results in high-strength cementitious networks (e.g., inorganic polymer binders) that account for the properties of structural materials.[1−5] Chemical/mechanical polishing (CMP) or planarization of metal oxide materials are important processes in the fabrication of semiconductor devices and often involve alkaline slurries of particles used to smooth the surfaces of much harder wafer materials.[6−10] More broadly, oxide materials used in heterogeneous catalysis or drug delivery applications can crystallize via dissolution and reprecipitation of precursor species in aqueous conditions.[11−17] In each of these examples, dissolution of surface silica or alumina species in aqueous environments is important to the development of macroscopic properties of interest, such as compressive and tensile strength in cements, resistance to corrosion in structural materials, increased material removal rates for semiconductor processing, or formation of pore structures in oxide catalysts.

Although inorganic oxide materials typically exhibit low dissolution rates, such rates have been observed to increase dramatically at confined asymmetric solid−liquid−solid interfaces. For example, the geological phenomenon known as "pressure solution" involves enhanced dissolution at mineral−mineral grain boundaries in the presence of water, such as at the interface between quartz and clays, including muscovite mica.[18−24] While pressure solution effects were previously attributed to high geologic pressures,[25,26] recent studies of dissolution in acidic and neutral solutions have shown that enhanced dissolution can occur for confined surfaces at ambient pressures and furthermore indicate that the rates of dissolution depend on the electrostatic potentials of

Special Issue: Intermolecular Forces and Interfacial Science

Received: July 2, 2019
Revised: August 14, 2019
Published: August 27, 2019

DOI: 10.1021/acs.langmuir.9b02043
Langmuir 2019, 35, 15651−15660

the two surfaces.[27,28] The electrochemical environment also influences corrosion at metal-mineral boundaries,[29,30] and other studies have described the influence of solution conditions (e.g., pH, ionic strength) and surface potential on the dissolution kinetics of isolated surfaces.[31−33] Although the dissolution kinetics of inorganic materials, including silicates and aluminates, under technologically relevant conditions have been widely studied, fundamental aspects that account for dissolution of these materials remain poorly understood,[34−39] especially under alkaline conditions that are specifically relevant to CMP and structural materials.[40] Furthermore, the impact of electrochemical considerations on the dissolution of oxide materials at asymmetric solid−liquid−solid interfaces in alkaline solutions has not been explored.

Here, quantitative analyses of the dissolution of amorphous silica and alumina at confined solid−liquid−solid interfaces in alkaline environments yield insights into the electrochemical factors that account for enhanced dissolution rates. Using an electrochemical pressure cell, the dissolution rate of silica in close proximity to a gold electrode under alkaline conditions is enhanced dramatically by changing the potential of the gold electrode. Using a surface forces apparatus (SFA), the dissolution rates were measured for alumina and silica particles confined between mica surfaces under the same alkaline conditions as the pressure cell. Dissolution of alumina and silica particles in close proximity to mica (silica−liquid−mica and alumina−liquid−mica interfaces) was enhanced relative to single-surface dissolution of silica or alumina in similar bulk solutions (silica−liquid and alumina−liquid interfaces). We propose that the dissolution enhancement results from changes in the electrostatic potential distribution between the asymmetric surfaces, due to overlap between electric double layers. The results and analyses manifest the importance of surface electrochemical properties and confinement, in addition to solution conditions, on the rates of dissolution of oxide surfaces. These can be applied to manipulate dissolution rates by several orders of magnitude, including for typically slow-dissolving alumina or silica materials, to dramatically increase or control the rates of processes that are important in microelectronics fabrication, the development of strength in structural materials, and catalyst syntheses.

EXPERIMENTAL SECTION

Dissolution of a silica surface in close proximity to a gold electrode was measured using a custom-built electrochemical pressure cell. The Teflon pressure cell had a total volume of approximately 200 mL. Two surfaces were arranged in a flat-on-flat geometry, aligned with a ball-and-socket joint on the top surface. The top surface was a gold electrode (roughness = 1 nm RMS) with a diameter of 10 mm prepared by template stripping from an atomically smooth mica surface, and this was connected to a potentiostat via a gold wire.[41,42] The bottom surface was an approximately 500 nm thick SiO_2 film, (roughness = 1 nm RMS) deposited on a silicon wafer via ion beam deposition with thickness measured by ellipsometry (J.A. Woollam Co.). The bottom surface was spring loaded, and the applied force was measured with strain gauges. The top surface was slightly off-center to allow contact of the gold wire, resulting in a 0.7 cm^2 silica−gold contact area. The surfaces were held in contact throughout the experiment at a pressure of 2−3 atm, calculated from the applied force divided by the contact area. A potentiostat (Gamry, Model Reference 3000) was used to control the surface potential of the gold working electrode in a three-electrode configuration, with a platinum mesh counter electrode and a AglAgCl reference electrode. For each silica dissolution experiment, the pressure cell was filled with alkaline aqueous solution, pH 10, prepared using NaOH (Sigma-Aldrich, ≥ 98%). The silica was allowed to dissolve for 24 h at each applied potential. After dissolution, the thickness of the silica layer was measured with ellipsometry. The average dissolution rate was calculated by dividing the change in silica thickness by the 24-h time interval.

Particle dissolution experiments were also conducted in which silica or alumina nanoparticles in aqueous alkaline solutions were compressed between two mica surfaces in a surface forces apparatus (SFA), model SFA2000 (SurForce, LLC). Suspensions of amorphous silica (SiO_2) nanoparticles (diameter = 200 ± 50 nm) (US Research Nanomaterials) were prepared at 25−50 wt % in alkaline solutions (0.1 mM NaOH, pH 10 and 1 mM NaOH, 10 mM NaCl, pH 11). A suspension of amorphous alumina (Al_2O_3) nanoparticles (diameter = 50 ± 5 nm) (US Research Nanomaterials, 99.8% trace metals basis) was prepared at 25−50 wt % in an alkaline solution (0.1 mM NaOH, pH 10). All suspensions were prepared with deionized water (3 MΩ·cm, TOC < 7 ppb). For each experiment, a nanoparticle suspension was injected between two freshly cleaved muscovite mica surfaces arranged in a crossed cylinder geometry. The distance between the mica surfaces was measured with multiple beam interferometry and was controlled with a piezoelectric crystal or micrometer. The deflection of a double cantilever spring was used to determine the normal force between the surfaces. The surfaces were brought into contact with 1−3 nanoparticles in the contact area, and the SFA chamber (∼200 mL) was then filled with alkaline solution of the same pH and salt concentration as the nanoparticle suspension solution. The average pressure across the contact was approximately 110 atm, calculated from the radius of the contact area by assuming Hertzian mechanics, described in the Supporting Information (S1). Confined particles distort the mica surfaces and shift the interference fringes. The change in wavelength of the interference fringes is used to calculate the particle diameter (d). The difference between the initial particle diameter, d_0, and the particle diameter normal to the confining surfaces measured as a function of time, $d(t)$, corresponds to the change in particle diameter, $\Delta d = d(t) - d_0$. The uncertainty of each data point is ±3 Å, calculated from the standard deviation of collections of points with unchanging particle diameter. Change in particle diameter corresponds to dissolution of the particles. In each particle dissolution experiment, a delay of 2 ± 1 min occurs after confinement of the particles before measuring the particle diameter due to the time required for adjustment of the optics in the SFA. For the SFA analyses presented here, the diameters of the silica or alumina particles are measured more conveniently and accurately than the distance between the mica and the silica or alumina particle surfaces, which can be subsequently estimated by using the local pressure, surface roughness, surface hydration, and concentration of adsorbed ions.[42] The high local pressure at the surface of the trapped particle (Supporting Information, S2) will result in short separation distances down to atomic contact (D < 3 Å) between a particle and the mica surface, where enhanced dissolution is expected to occur. All experiments were conducted at room temperature (22 °C). A schematic diagram of the SFA experimental setup and pictures of the interference fringes taken before and after confinement of the nanoparticles are shown in Figure S1, and additional details of SFA operation are given elsewhere.[43]

RESULTS AND DISCUSSION

We hypothesize that dissolution is enhanced by electrochemical effects that arise from differences in the electrostatic potentials of different surfaces in nanoscale proximity. To test this hypothesis, a custom-built electrochemical pressure cell was used to measure the dissolution rate of an extended silica surface in contact with a gold electrode at different controlled potentials in an alkaline solution (0.1 mM NaOH, pH 10). Figure 1A shows a schematic diagram of the pressure cell configuration. Constant electrostatic potentials were applied to the gold surface over 24-h periods, during which dissolution occurred and the silica film thickness decreased. Figure 1B

DOI: 10.1021/acs.langmuir.9b02043
Langmuir 2019, 35, 15651−15660

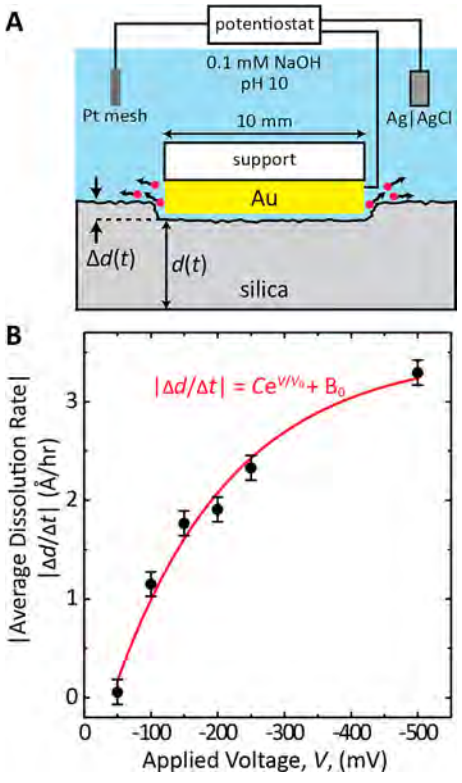

Figure 1. (A) Schematic diagram of the electrochemical pressure cell used to measure the dissolution of a flat silica surface in close proximity to a gold electrode at various applied surface potentials in an alkaline solution (0.1 mM NaOH, pH 10). The three-electrode setup included a Au working electrode, a Pt mesh counter electrode, and a Ag|AgCl reference electrode. The red circles indicate silicate ions diffusing away from the dissolution region. (B) Absolute value of the average dissolution rate determined from measured changes in silica film thickness, $\Delta d(t)$, after 24-h dissolution periods, Δt, at each applied potential (V). Uncertainty bars are associated principally with the ellipsometry measurement of silica thickness (±3 Å). The red line indicates an exponential fit to the data with equation parameters given in the text.

shows a plot of the absolute value of the dissolution rate of a silica film exposed to an alkaline solution and in nanoscale proximity to a gold surface to which different negative potentials have been applied. Under these conditions, the potential applied to the gold surface does not correspond directly to the Stern or ζ potentials of that surface, which are influenced by ion adsorption. In addition, the average pressure (2−3 atm) was significantly less than the pressures (>100 atm) that have previously been considered to be responsible for enhanced dissolution under more geologically relevant conditions.[25,26] The absolute value of the silica dissolution rate increases with increasingly negative applied potentials (V) at the gold electrode and is described by the empirical equation $|\Delta d/\Delta t| = C \times \exp(V/V_0) + B_0$ where V_0 = 180 mV, C = −4.4 Å/h, and B_0 = 3.5 Å/h. The empirical model was used to fit the measured dissolution rates that result from a combination of reaction kinetics, diffusion limitations, and electrochemical response of the system.

As shown in Figure 1B, the absolute value of average dissolution rate of the silica surface increases by over an order of magnitude over the range of negative potentials applied to the gold electrode (−50 to −500 mV). The results suggest that the absolute value of the dissolution rate approaches an upper limit at large negative potentials of the gold electrode. This is consistent with transport limitations becoming important at high dissolution rates within the highly confined nanoscale-separated surfaces and large interfacial contact area.[44] At high dissolution rates, slow diffusion can become rate-limiting, accompanied by a buildup of dissolved silicate species that can impede further dissolution. Ion diffusion may also be complicated by the formation of pits and surface roughening.[27] Regardless of whether diffusion limitations contribute, the dependence of silica dissolution rate on the potential applied to another nearby surface in close proximity at low pressure (2−3 atm) and ambient temperature (298 K) demonstrates that the electrochemical environment contributes importantly to enhanced rates of dissolution.

The dissolution rates of silica and alumina particles in aqueous alkaline solution conditions are also increased by proximity to muscovite mica, demonstrating that close proximity to a surface with different electrostatic potential influences dissolution kinetics even for nonconducting materials. For the particle dissolution experiments, silica or alumina nanoparticles (20−300 nm in diameter) in aqueous solutions were compressed between two extended mica surfaces using a surface forces apparatus (SFA). The nanoparticles were confined between the mica surfaces in alkaline solutions of pH 10 or 11, during which the particle diameters were measured as functions of time (Figure 2). As a particle dissolves, its diameter normal to the confining surfaces

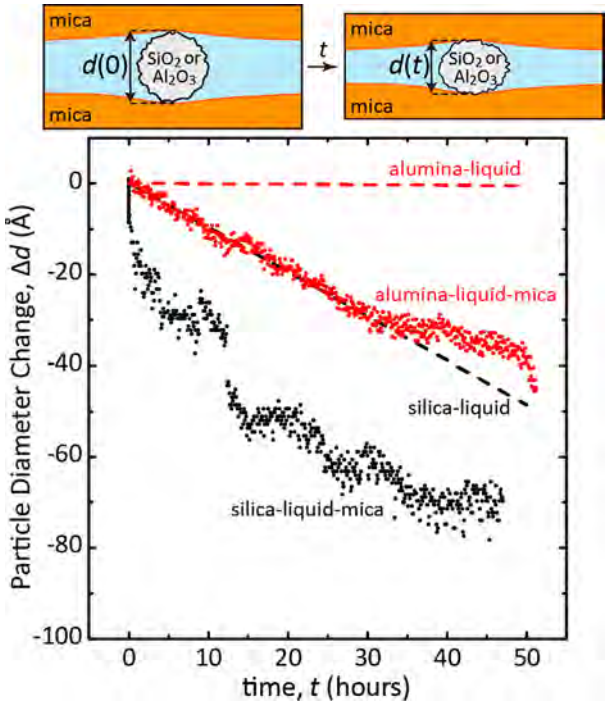

Figure 2. Plots of measured changes in nanoparticle diameter, $\Delta d = d(t) - d(0)$, as functions of time for mica-confined spherical amorphous silica particles (silica-liquid-mica) and alumina particles (alumina-liquid-mica) in an alkaline solution (0.1 mM NaOH, pH 10). The uncertainty of each data point is ±3 Å. The dashed lines show the single-surface dissolution rates reported in the literature for isolated silica[46] (silica-liquid) and alumina[33] (alumina-liquid) surfaces at the same bulk solution conditions. The proximity to a mica surface increases the dissolution rate of both the silica and alumina nanoparticles, though to different extents.

DOI: 10.1021/acs.langmuir.9b02043
Langmuir 2019, 35, 15651−15660

decreases. The confined silica and alumina nanoparticles exhibited larger dissolution rates than literature dissolution rates for isolated silica[46] and alumina[33] surfaces in the same bulk solution conditions.

Enhanced dissolution occurs upon introduction of a surface (in this case mica) that has a more negative ζ potential than the dissolving surface. For example, at pH 10, ranges of ζ potentials have been measured for alumina (−10 to −60 mV),[47−49] amorphous silica (−50 to −120 mV),[50−55] and mica (−80 to −160 mV).[55−59] The ζ potentials (the potential at the slipping plane of the surface) are compared, rather than the surface or Stern potentials, because the ζ potential is more experimentally accessible and widely reported.[60−62] The relationship between the electrochemical dissolution rate and the single-surface dissolution rate can be represented by the enhancement factor (ε), defined as $\varepsilon = \Delta d_{\text{measured}}/\Delta d_{\text{single-surface}}$. The enhancement factor provides a means for quantifying and comparing the influences of asymmetric confined interfaces on the rates of dissolution (both actual and relative) for different materials, such as silica and alumina, which exhibit different single-surface dissolution rates under otherwise identical solution conditions. For example, the average dissolution rate over 51 h of an alumina particle confined between mica surfaces is measured to be 0.9 Å/h (Figure 2, alumina−liquid−mica), while the reported dissolution rate[33] of isolated alumina surfaces under the same solution conditions is approximately 0.01 Å/h (Figure 2, alumina−liquid), yielding an enhancement $\varepsilon = 90$. Therefore, the dissolution rate of alumina increased by 2 orders of magnitude when confined between mica surfaces compared to a single surface exposed to bulk solution. The initial dissolution rate over 5 h of an amorphous silica nanoparticle confined between mica surfaces was 6 Å/h (Figure 2, silica−liquid−mica), yielding an enhancement $\varepsilon = 6$ over the reported dissolution rate (1.0 Å/h)[46] of isolated amorphous silica surfaces in the same solution conditions (Figure 2, silica−liquid). The average dissolution rate over 47 h was 1.5 Å/h, yielding an enhancement $\varepsilon = 2$ over the reported single-surface dissolution rate. For comparison, the maximum dissolution rate measured for silica in close proximity to a gold electrode (Figure 1B) cell was 3.3 Å/h, yielding an enhancement $\varepsilon = 3$. The dissolution of a silica particle confined between mica surfaces is compared to the dissolution of an extended silica surface in close proximity to a gold electrode (Figure 1) in Figure S2. The silica particle also exhibited rapid dissolution at early times ($t < 1$ h), similar to the previously observed rapid initial dissolution of extended silica surfaces in close proximity to a gold electrode, attributed to formation and saturation of an interfacial film of dissolved silica.[28] The silica nanoparticle dissolved through repeated cycles of rapid dissolution followed by greatly reduced dissolution, previously attributed[27] to collapse of surface pits in dissolution studies of quartz in close proximity to mica in acidic solutions.

As for the dissolution of extended silica surfaces, silica particle dissolution in confined environments is often also limited by diffusion of dissolved species. Compared to those under previous acidic or neutral solution conditions, diffusion limitations here are expected to be more pronounced under conditions favoring silica dissolution (e.g., alkaline saline solutions), which promote relatively high local concentrations of soluble silica species near the surfaces. The dissolution of a silica particle in a strongly alkaline saline solution (1 mM NaOH, 10 mM NaCl, pH 11) is shown in Figure 3. Solution

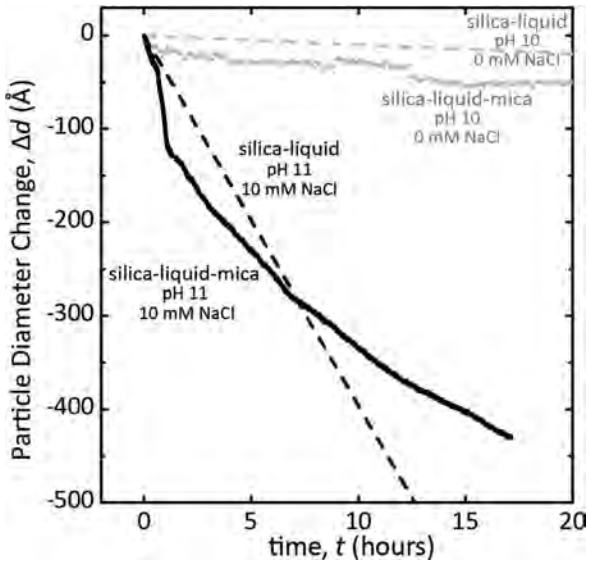

Figure 3. Plots of measured changes in nanoparticle diameter, $\Delta d = d(t) - d(0)$, as functions of time for mica-confined silica particles (silica-liquid-mica) under different alkaline solution conditions: (gray, from Figure 2) 0.1 mM NaOH, pH 10 and (black) 1 mM NaOH, 10 mM NaCl, pH 11. The dissolution rates reported for isolated amorphous silica surfaces under the respective bulk solution conditions are shown by the dashed lines: (gray) from reference 46 (black) from reference 39.

conditions were chosen to enable comparison with literature studies[39,63] on dissolution of isolated silica surfaces. We note that the coupled effects of pH and ionic strength on the rates of dissolution in confined nanoscale geometries are complicated. Nevertheless, mica is expected to have a more negative potential than silica under these solution conditions,[55] and significant dissolution enhancement is observed. The initial and early stage ($t < 100$ min) dissolution rates of silica particles in close proximity to a mica surface are much higher than the dissolution rate of isolated surfaces of the same material ($\varepsilon > 0$). By comparison, at longer times ($t > 100$ min), the single-surface dissolution rate is larger ($\varepsilon < 0$). The decrease in the dissolution rate of the silica particle over time can be attributed to the diffusion limitations and local saturation of dissolved silicate species that were proposed to occur in the pressure cell experiments discussed previously. In the dissolution processes examined here, the particles were confined between two mica surfaces and dissolved species must diffuse through the gap containing the particle to the bulk solution, as described by Alcantar et al. for a related system.[26] Transport through the gap is expected to be limited by the relatively high pressure in the contact area and the small mica−mica separation around the trapped particle. Such inhibited transport may result in local saturation of the soluble silicate species, and correspondingly, a reduced rate of dissolution, as discussed in the Supporting Information (S3). Dissolution of single isolated surfaces is expected to be generally less transport-limited, so the dissolution rate of isolated surfaces could be higher than the dissolution rate of confined surfaces over long time periods, depending on confinement dimensions, geometry, solution conditions, and the electrochemical properties of the surfaces.

The experimental results establish that dissolution at confined solid−liquid−solid surfaces in alkaline solutions depends on the potential difference between electrochemically dissimilar surfaces in close proximity. Previous studies have

DOI: 10.1021/acs.langmuir.9b02043
Langmuir 2019, 35, 15651−15660

attributed enhanced dissolution at confined interfaces to an overlap of electric double layers that increases the concentration of cations at the dissolving surface; these cations are thought to promote dissolution by lowering the energy barrier to dissolution.[27,28] However, enhanced dissolution is not observed for symmetric charged surfaces in close proximity,[27] despite the increased cation concentration expected at each surface that results from overlapping symmetric double layers, suggesting that locally higher cation concentrations cannot fully account for enhanced dissolution at confined solid−liquid−solid interfaces. We propose an alternative model for the electrochemically enhanced dissolution of metal oxides that involves a change in the direction of the electric field at the dissolving surface that influences the reaction pathway and lowers the energy barrier to dissolution.

An electrically charged surface (or surface with nonzero electrostatic potential) in an electrolyte solution causes the ions in solution to arrange in an electric double layer that balances the surface charge. Some of the surface charge is balanced by counterions of opposite charge that are bound to the surface within the Stern or Helmholtz layer; the remainder of the surface charge is balanced by an increased concentration of counterions in solution close to the surface, known as the diffuse electric double layer, the distribution of which follows the Poisson−Boltzmann equation.[64] The Debye length is the characteristic dimension of the diffuse electric double layer and depends only on the properties of the bulk solution. The Debye length (κ^{-1}) can be expressed as follows, simplified from the Grahame equation for a monovalent electrolyte at 25 °C:[64] $\kappa^{-1} = (\varepsilon_0 \epsilon kT/2\rho_\infty e^2)^{1/2} = 0.304 \times 10^{-9}/M^{1/2}$, where ϵ_0 is the dielectric permittivity of free space, ϵ is the bulk dielectric permittivity of the aqueous solution, k is the Boltzmann constant, T is the temperature, ρ_∞ is the concentration of ions in the bulk, e is the elementary charge of an electron, and M is the molar concentration of the monovalent electrolyte in the aqueous solution. Within the diffuse portion of the double layer, the electrostatic potential (ψ) decays exponentially from its maximum at the surface to zero within the bulk solution. The electric field (E) is the gradient of the electrostatic potential, $E = d\psi/dx$, where x is the coordinate normal to the surface. When two charged surfaces are brought into close proximity, their electric double layers overlap, and the potential between the surfaces is given by the Hogg-Healy-Fuerstenau equation for electrostatic potential for dissimilar surfaces:[65] $\psi = \psi_1 \cosh(\kappa x) + \sinh(\kappa x)[(\psi_2 - \psi_1 \cosh(2\kappa D))/\sinh(2\kappa D)]$, where ψ_1 and ψ_2 are the potentials of the surfaces, κ is the inverse Debye length, D is the distance separating the two surfaces, and x is the distance from the midpoint between the surfaces. We note that the Hogg-Healy-Fuerstenau equation assumes that the surfaces are at equilibrium with constant surface potentials and is most accurate for low surface potentials (ψ_i < 25 mV) and large separations ($D > 1\ \kappa^{-1}$). However, even for large potentials (ψ_i > 150 mV) and large potential differences between the surfaces ($|\psi_2 - \psi_1|$ > 150 mV), the estimated errors in free energy calculations for ($D < \kappa^{-1}$) are less than 10%.[65] The Hogg-Healy-Fuerstenau equation used here provides an approximation of the potential distribution between the surfaces assuming pseudoequilibrium and constant surface potentials. However, for nanoscale separation distances in confined solid−liquid−solid interfaces, the potential at each surface can differ from that expected for bulk equilibrium conditions and can also vary transiently with separation distance as ions are forced onto the surface, a process called "charge regulation".[64] While there are more complicated models for interactions between surfaces that account for charge regulation[66] and specific ion-surface interactions,[67] these models also usually assume equilibrium conditions. To our knowledge, no model has fully incorporated the relationships between electrostatic potentials, solution conditions, and dissolution of oxide materials, in part because the dissolution mechanisms of these materials are not well understood.

For two surfaces with different surface potentials under a given set of conditions, a decrease in separation distance can result in a reversal of the electric field direction at the surface with the less-negative potential. This occurs specifically when the derivative of the electrostatic potential with respect to position changes sign. To illustrate this reversal in electric field direction, Figure 4A shows plots of the electrostatic potential as a function of the position x_i across an alumina−liquid−mica interface for various surface separation distances D_i relative to the Debye length κ^{-1}. For large separation distances (e.g., $D_1 = 8\kappa^{-1}$, black), the electrostatic potential increases from the potential at the less-negative alumina surface (−20 mV at $x_1 = 0$) to nearly zero (close to the bulk solution potential) and then decreases again to the potential at the more-negative mica surface (−110 mV at $x_1 = D_1$). Similarly, the electrostatic potential plotted for a smaller separation distance ($D_2 = 4\kappa^{-1}$, red) increases with increasing position away from the less-negative surface and then decreases at positions closer to the more-negative surface. In contrast, the electrostatic potential plotted for an even smaller separation distance ($D_3 = 2\kappa^{-1}$, blue) decreases monotonically from the less-negative surface to the more-negative surface. Finally, the electrostatic potential between surfaces separated by a single Debye length ($D_4 = \kappa^{-1}$, green) decreases almost linearly from the less-negative alumina surface to the more-negative mica surface.

The electric field (E) corresponds to the first derivative of the electrostatic potential with respect to the position (x_i) between two surfaces. Figure 4B shows plots of the electric field, normalized by the magnitude of the largest electric field (E_{max}), as a function of position x_i for the same separation distances D_i as in Figure 4A. For large separation distances (e.g., $D_1 = 8\kappa^{-1}$, black), the normalized electric field at the less-negative alumina surface ($x_1 = 0$) is negative, indicating that the electric field is directed toward that surface. By comparison, the normalized electric field at the more-negative mica surface ($x_1 = D_1$) is positive, indicating that the electric field is directed toward that surface. Similarly, for $D_2 = 4\kappa^{-1}$ (red), the electric fields at each surface point toward their nearest surface. In contrast, when the separation distance is decreased further to $D_3 = 2\kappa^{-1}$ (blue) or $D_4 = \kappa^{-1}$ (green), the electric field is positive at all positions, indicating that the electric field is directed toward the more-negative mica surface at all positions x_i. Importantly, the electric field at the less-negative surface points toward that surface at large separation distances and away from the surface at small separation distances, under otherwise identical conditions. Therefore, as separation distance decreases, the direction of the electric field at the less-negative surface reverses, and dissolution is expected to be enhanced.

The materials and solution conditions used in this work are expected to result in reversed electric fields at the less negative surface for asymmetric confined solid−liquid−solid interfaces. Figure 5 shows the electrostatic potential as a function of position (x) predicted by the Hogg-Healy-Fuerstenau equation

DOI: 10.1021/acs.langmuir.9b02043
Langmuir 2019, 35, 15651−15660

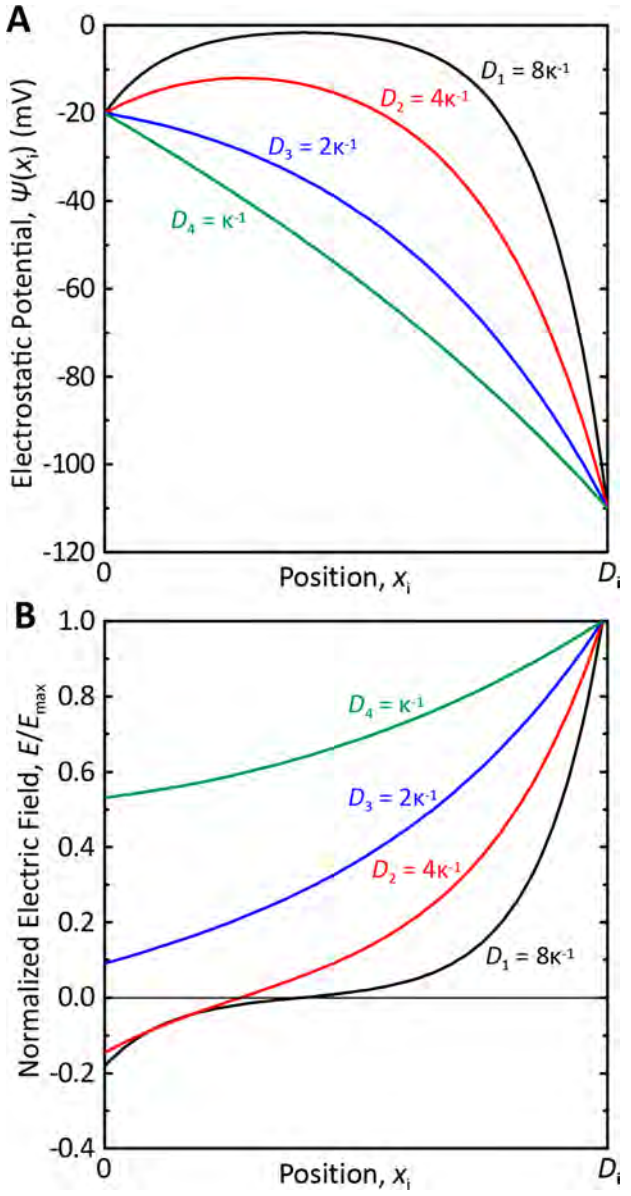

Figure 4. (A) Plots of the electrostatic potential between alumina (−20 mV) and mica (−110 mV) surfaces versus position (x_i) for a range of separation distances (D_i) from $8\kappa^{-1}$ to κ^{-1} under alkaline conditions. (B) Plots of the normalized electric field versus position (x_i) for the same separation distances (D_i) and alkaline conditions as in part A.

for solid−liquid−solid interfaces involving pairs of materials in close proximity (4 nm separation) under alkaline solution conditions (0.1 mM NaOH, pH 10). This surface separation is much less than the Debye length (κ^{-1}) of 30 nm given by the Grahame equation for this solution (0.1 mM NaOH). For a symmetric mica−liquid−mica pair of surfaces, the electrostatic potential distribution (black dashed line) across the liquid gap is approximately constant, and the electric field is therefore close to zero. By comparison, for a silica−liquid−mica configuration under otherwise identical conditions (green dashed line), the electrostatic potential decreases monotonically from the less- to the more-negative surface. This electrostatic potential distribution corresponds to an electric field that is directed away from the less-negative silica surface, and which is opposite to the direction of the electric field when

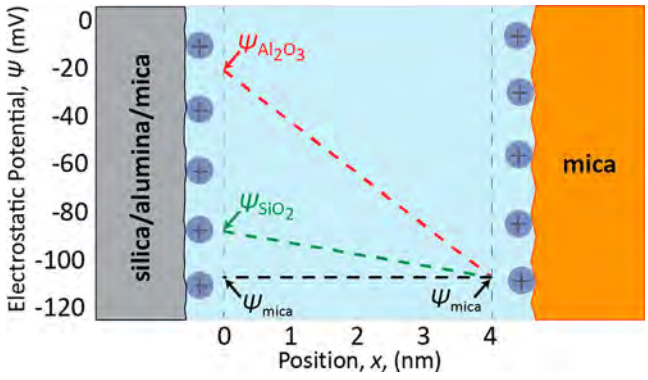

Figure 5. Schematic diagram of the electrostatic potential distributions, as predicted by the Hogg-Healy-Fuerstenau equation, between pairs of surfaces in an alkaline solution (0.1 mM NaOH, pH 10) and for a 4 nm separation distance. The left surface is alumina, silica, or mica, with ζ potentials of −20, −90, and −110 mV, respectively, and the right surface is mica. ζ potentials are the electrostatic potentials at the slipping plane at the surface (light blue dashed lines). The ζ potentials shown here are representative values within the range given in the literature, described in the text. The density of adsorbed cations on each surface depends on the material properties and solution composition.

the surfaces are well-separated ($D_i > 3\ \kappa^{-1}$ as shown in Figure 4). Similarly, an alumina−liquid−mica configuration (red dashed line) exhibits a monotonic decrease in potential from the less- to the more-negative surface, also corresponding to an electric field that is directed toward the more-negative mica surface. The potential gradient of the alumina−liquid−mica configuration is steeper than the gradient of the silica−liquid−mica configuration, consistent with the greater relative magnitude by which dissolution is enhanced at an alumina−liquid−mica interface compared to a silica−liquid−mica interface (Figure 2).

While silica and alumina dissolution mechanisms are not fully understood, the reactants, intermediate products, and products involve charged species.[36,39] In the proposed model, the reversed electric field direction at the alumina or silica surface in close proximity to mica promotes bond polarization and/or ion release during dissolution. For cases where dissolution reactions are rate-limiting, the reversal of the electric field is expected to increase the dissolution rate. An analogous situation is the application of tensile force to a bond that reduces the bond lifetime, a phenomenon described by the Bell theory.[68] For the case of enhanced dissolution, the change in electric field magnitude and direction can influence dissolution by changing the concentration of ions available for reaction at the surface, the effective activation energy of the dissolution reaction, and the local saturation of dissolved species (if or when mass transport of the dissolved ions away from the surface becomes limiting). Our proposed model for the dissolution-enhancement process is depicted schematically in Figure 6 for a silica−liquid−mica interface. When the mica and silica surfaces are separated by a large distance $D \gg \kappa^{-1}$ ($t < 0$, Figure 6A), the electric double layers of each surface do not overlap and the dissolution rate is expected to be the rate of a single isolated surface in bulk solution (silica−liquid configuration). At $t = 0$ (Figure 6B), the surfaces are brought into close proximity ($D < \kappa^{-1}$), such that their electrochemically asymmetric diffuse layers overlap, causing the direction of the electric field at the less negatively charged surface to be

DOI: 10.1021/acs.langmuir.9b02043
Langmuir 2019, 35, 15651−15660

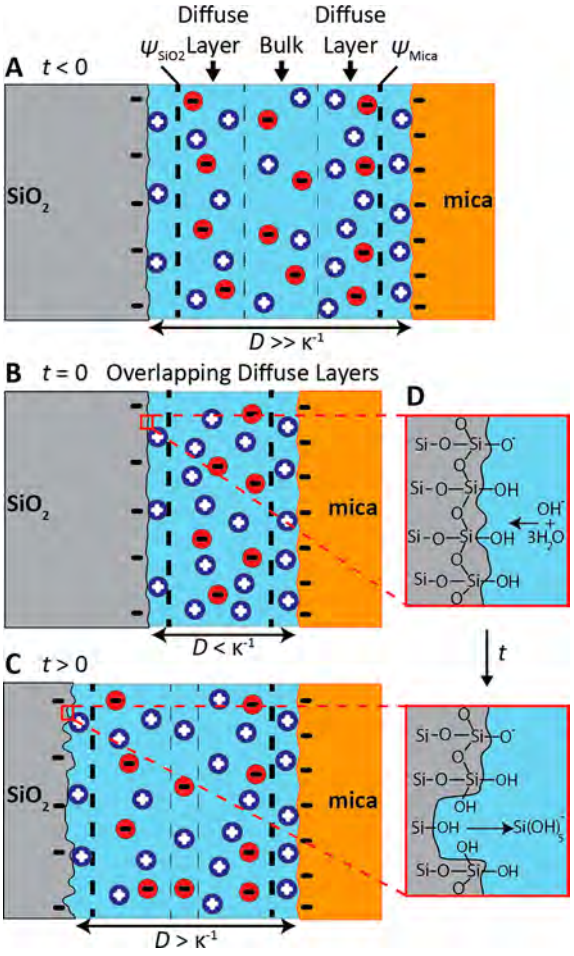

Figure 6. Schematic representation of the proposed model of electrochemically enhanced dissolution from two dissimilar surfaces, here silica and mica. The ζ potential of each surface is the potential at the slipping plane, indicated by the thick dashed lines. (A) For large separation distances ($D \gg \kappa^{-1}$), dissolution of silica is not enhanced. (B) At $t > 0$, the surfaces are brought into close proximity ($D < \kappa^{-1}$) and the diffuse portions of the electric double layers at each surface overlap across the asymmetric solid–liquid–solid interface, reversing the electric field at the surface with the less negative potential. In this case, silica dissolves by successive hydrolysis reactions as shown schematically in the inset. (C) As time progress ($t > 0$), the surface with the less negative potential will undergo enhanced dissolution until the surfaces are well-separated and dissolution returns to the single-surface dissolution rate. (D) Dissolution reaction of silica in an alkaline environment consistent with a mechanism proposed by Iler.[34]

reversed. For $t > 0$ (Figure 6C), dissolution is enhanced by the reversed electric field, leading to preferential removal of material from the less negatively charged surface, as depicted schematically in Figure 6D. For the case where the bulk silica and mica substrates are held fixed with time, enhanced dissolution will continue until the separation distance increases to the point that the Debye layers no longer overlap, and single-surface dissolution rates are re-established. For the case where the bulk silica and mica substrates are maintained in close proximity as dissolution occurs (e.g., in the SFA and electrochemical pressure cell measurements conducted here), an enhanced dissolution rate will be sustained though it may be limited by transport effects that can result in local saturation of dissolved species near the confined surfaces.

Our results demonstrate that surface potentials influence dissolution processes in confined environments, which we attribute to a reversal in the direction of the electric field at the less-negatively charged dissolving surface. For a constant surface separation, the model predicts that decreasing the Debye length (e.g., by increasing the ionic strength) will reduce the extent of overlap between the double layers of the respective surfaces and therefore reduce the rate of dissolution. This prediction is consistent with the results in Figure 3 showing that a reduction in the Debye length from 30 to 3 nm reduces the initial rate of dissolution of amorphous silica ($\varepsilon = 6$ to $\varepsilon = 2$). Such predictions are based on a continuum description of the electrochemical environment, with the potential distribution and electric field resulting from an average of the potentials associated with charged molecular species. Alternatively, enhanced dissolution at confined interfaces can be approached from an atomistic description of the environment near the dissolving surface, e.g., resulting from the effects of increased cation concentrations at the dissolving surface result from the overlapping double layers.[27,28] Establishing the conditions, criteria, and limitations of the continuum and atomistic models presents opportunities to increase understanding of enhanced dissolution over complementary length scales.

CONCLUSIONS

By manipulating the electrostatic potential applied to a gold electrode in close proximity to a silica surface, the dissolution rate of silica was increased by an order of magnitude. Furthermore, silica and alumina nanoparticles in close proximity to a dissimilar nonconducting material are shown to exhibit dissolution rates that are up to 2 orders of magnitude larger than the dissolution rates of isolated surfaces under otherwise identical bulk solution conditions. The results demonstrate the crucial role of electrochemical interactions in enhanced dissolution: overlapping double layers of dissimilar surfaces in nanoscale proximity result in reversed electric fields that facilitate the removal of ions from the surfaces, resulting in dramatically enhanced rates of dissolution. We demonstrate that transport limitations can influence dissolution kinetics of a silica surface in nanoscale proximity to a gold electrode held at a large negative potential and that transport limitations also influence dissolution kinetics of silica particles confined between mica surfaces. Therefore, convective transport of ions away from the surfaces (as occurs in chemical/mechanical polishing processes) is expected to result in high dissolution rates. Further analyses of the mechanisms of silica and alumina dissolution are currently underway in our laboratory, including the coupled effects of pH and ionic strength on the rates of dissolution in confined nanoscale geometries and the effects of convective transport on dissolution kinetics. Broadly, the results provide new insights on the factors that influence dissolution kinetics in confined aqueous–solid environments, in particular, surface electrochemical properties. The insights are expected to be general and lead to improved control of dissolution, precipitation, crystallization, of surface-restructuring processes that are important in chemical/mechanical polishing, syntheses of heterogeneous catalysts, and the rheology and development of strength of structural materials.

DOI: 10.1021/acs.langmuir.9b02043
Langmuir 2019, 35, 15651–15660

■ ASSOCIATED CONTENT

Supporting Information

The Supporting Information is available free of charge on the ACS Publications website at DOI: 10.1021/acs.langmuir.9b02043.

Approximation of the average pressure of the contact area, approximation of the local pressure at the surface of a confined nanoparticle, schematic of SFA experimental setup, dissolution of an amorphous silica surface in close proximity to a gold electrode, saturation of the volume around a confined dissolving nanoparticle (PDF)

■ AUTHOR INFORMATION

Corresponding Author

*E-mail: bradc@engineering.ucsb.edu.

ORCID

Kai Kristiansen: 0000-0002-7555-9437
Tandré Oey: 0000-0002-9004-399X
Gaurav Sant: 0000-0002-1124-5498
Bradley F. Chmelka: 0000-0002-4450-6949
Jacob N. Israelachvili: 0000-0001-8915-8741

Present Address

●Department of Chemistry and Applied Biosciences, ETH Zurich, 8093 Zürich, Switzerland.

Author Contributions

¶H.A.D. and G.D.D. contributed equally.

Notes

The authors declare no competing financial interest.

■ ACKNOWLEDGMENTS

This project was primarily supported by the U.S. Department of Transportation (U.S. DOT) through the Federal Highway Administration under Award # DTFH61-13-H-00011: K.K., A.M.S., and Z.J.B. acknowledge partial financial support from the U.S. Department of Energy (DOE), Office of Science, Basic Energy Sciences (BES), under Award # DE-FG02-87ER-45331. G.D.D. was supported by the National Science Foundation Graduate Research Fellowship Program under Grant No. 1650114. Any opinions, findings, and conclusions or recommendations expressed in this material are those of the authors and do not necessarily reflect the views of the National Science Foundation. The authors thank B. Abrams for assistance with the electrochemical pressure cell measurements. The silica surfaces for the electrochemical pressure cell were fabricated in the University of California Santa Barbara (UCSB) nanofabrication facility, part of the NSF funded National Nanotechnology Infrastructure Network (NNIN) network.

■ REFERENCES

(1) Duxson, P.; Fernández-Jiménez, A.; Provis, J. L.; Lukey, G. C.; Palomo, A.; Van Deventer, J. S. J. Geopolymer Technology: The Current State of the Art. *J. Mater. Sci.* **2007**, *42* (9), 2917−2933.

(2) Hajimohammadi, A.; Provis, J. L.; Van Deventer, J. S. J. Effect of Alumina Release Rate on the Mechanism of Geopolymer Gel Formation. *Chem. Mater.* **2010**, *22* (18), 5199−5208.

(3) Björnström, J.; Martinelli, A.; Matic, A.; Börjesson, L.; Panas, I. Accelerating Effects of Colloidal Nano-Silica for Beneficial Calcium-Silicate-Hydrate Formation in Cement. *Chem. Phys. Lett.* **2004**, *392* (1−3), 242−248.

(4) Brand, A. S.; Bullard, J. W. Dissolution Kinetics of Cubic Tricalcium Aluminate Measured by Digital Holographic Microscopy. *Langmuir* **2017**, *33* (38), 9645−9656.

(5) Sangodkar, R. P.; Smith, B. J.; Gajan, D.; Rossini, A. J.; Roberts, L. R.; Funkhouser, G. P.; Lesage, A.; Emsley, L.; Chmelka, B. F. Influences of Dilute Organic Adsorbates on the Hydration of Low-Surface-Area Silicates. *J. Am. Chem. Soc.* **2015**, *137* (25), 8096−8112.

(6) Steigerwald, J. M.; Murarka, S. P.; Gutmann, R. J. *Chemical Mechanical Planarization of Microelectronic Materials*; Wiley: 2007.

(7) Nair, R. R.; Gupta, A.; Victoria, S. N.; Manivannan, R. Chemical Mechanical Planarization of Germanium Using Oxone® Based Silica Slurries. *Wear* **2017**, *376−377*, 86−90.

(8) Zhou, Y.; Pan, G.; Shi, X.; Zhang, S.; Gong, H.; Luo, G. Effects of Ultra-Smooth Surface Atomic Step Morphology on Chemical Mechanical Polishing (CMP) Performances of Sapphire and SiC Wafers. *Tribol. Int.* **2015**, *87*, 145−150.

(9) Zhang, Z.; Wang, B.; Zhou, P.; Kang, R.; Zhang, B.; Guo, D. A Novel Approach of Chemical Mechanical Polishing for Cadmium Zinc Telluride Wafers. *Sci. Rep.* **2016**, *6* (1), 26891.

(10) Krishnan, M.; Nalaskowski, J. W.; Cook, L. M. Chemical Mechanical Planarization: Slurry Chemistry, Materials, and Mechanisms. *Chem. Rev.* **2010**, *110* (1), 178−204.

(11) De Yoreo, J. J.; Gilbert, P. U. P. A.; Sommerdijk, N. A. J. M.; Penn, R. L.; Whitelam, S.; Joester, D.; Zhang, H.; Rimer, J. D.; Navrotsky, A.; Banfield, J. F.; Wallace, A. F.; Michel, F. M.; Meldrum, F. C.; Cölfen, H.; Dove, P. M. Crystallization by Particle Attachment in Synthetic, Biogenic, and Geologic Environments. *Science* **2015**, *349* (6247), aaa6760.

(12) Zhai, D.; Zhao, L.; Liu, Y.; Xu, J.; Shen, B.; Gao, J. Dissolution and Absorption: A Molecular Mechanism of Mesopore Formation in Alkaline Treatment of Zeolite. *Chem. Mater.* **2015**, *27* (1), 67−74.

(13) Carrier, X.; Lambert, J. F.; Che, M. Ligand-Promoted Alumina Dissolution in the Preparation of MoO_x/γ-Al_2O_3 Catalysts: Evidence for the Formation and Deposition of an Anderson-Type Alumino Heteropolymolybdate. *J. Am. Chem. Soc.* **1997**, *7863* (13), 10137−10146.

(14) Piana, S.; Gale, J. D. Understanding the Barriers to Crystal Growth: Dynamical Simulation of the Dissolution and Growth of Urea from Aqueous Solution. *J. Am. Chem. Soc.* **2005**, *127* (6), 1975−1982.

(15) Sindoro, M.; Yanai, N.; Jee, A. Y.; Granick, S. Colloidal-Sized Metal-Organic Frameworks: Synthesis and Applications. *Acc. Chem. Res.* **2014**, *47* (2), 459−469.

(16) Xu, L.; Ji, X.; Jiang, J. G.; Han, L.; Che, S.; Wu, P. Intergrown Zeolite MWW Polymorphs Prepared by the Rapid Dissolution-Recrystallization Route. *Chem. Mater.* **2015**, *27* (23), 7852−7860.

(17) Li, R.; Linares, N.; Sutjianto, J. G.; Chawla, A.; Garcia-Martinez, J.; Rimer, J. D. Ultrasmall Zeolite L Crystals Prepared from Highly Interdispersed Alkali-Silicate Precursors. *Angew. Chem., Int. Ed.* **2018**, *57* (35), 11283−11288.

(18) Bjorkum, P. A. How Important Is Pressure in Causing Dissolution of Quartz in Sandstones? *J. Sediment. Res.* **1996**, *66* (1), 147−154.

(19) Fisher, Q. J.; Knipe, R. J.; Worden, R. H. Microstructures of Deformed and Non-Deformed Sandstones from the North Sea: Implications for the Origins of Quartz Cement in Sandstones. In *Quartz Cementation in Sandstones*; Worden, R. H., Morad, S., Eds.; Blackwell Publishing Ltd.: 2009; pp 129−146.

(20) Heald, M. T. Stylolites in Sandstones. *J. Geol.* **1955**, *63* (2), 101−114.

(21) Heald, M. T. Cementation of Simpson and St. Peter Sandstones in Parts of Oklahoma, Arkansas, and Missouri. *J. Geol.* **1956**, *64* (1), 16−30.

(22) Houseknecht, D. W. Intergranular Pressure Solution in Four Quartzose Sandstones. *J. Sediment. Res.* **1988**, *58* (2), 228−246.

(23) Schwarz, S.; Stöckhert, B. Pressure Solution in Siliciclastic HP-LT Metamorphic Rocks — Constraints on the State of Stress in Deep Levels of Accretionary Complexes. *Tectonophysics* **1996**, *255* (3−4), 203−209.

DOI: 10.1021/acs.langmuir.9b02043
Langmuir 2019, 35, 15651−15660

(24) Weyl, P. K. Pressure Solution and the Force of Crystallization: A Phenomenological Theory. *J. Geophys. Res.* **1959**, *64* (11), 2001−2025.
(25) Green, H. W. "Pressure Solution" Creep: Some Causes and Mechanisms. *J. Geophys. Res.* **1984**, *89* (B6), 4313−4318.
(26) Alcantar, N.; Israelachvili, J.; Boles, J. Forces and Ionic Transport between Mica Surfaces: Implications for Pressure Solution. *Geochim. Cosmochim. Acta* **2003**, *67* (7), 1289−1304.
(27) Greene, G. W.; Kristiansen, K.; Meyer, E. E.; Boles, J. R.; Israelachvili, J. N. Role of Electrochemical Reactions in Pressure Solution. *Geochim. Cosmochim. Acta* **2009**, *73* (10), 2862−2874.
(28) Kristiansen, K.; Valtiner, M.; Greene, G. W.; Boles, J. R.; Israelachvili, J. N. Pressure Solution - The Importance of the Electrochemical Surface Potentials. *Geochim. Cosmochim. Acta* **2011**, *75* (22), 6882−6892.
(29) Ryan, M. P.; Williams, D. E.; Chater, R. J.; Hutton, B. M.; McPhail, D. S. Why Stainless Steel Corrodes. *Nature* **2002**, *415*, 770−774.
(30) Merola, C.; Cheng, H.-W.; Schwenzfeier, K.; Kristiansen, K.; Chen, Y.-J.; Dobbs, H. A.; Israelachvili, J. N.; Valtiner, M. In Situ Nano- to Microscopic Imaging and Growth Mechanism of Electrochemical Dissolution (e.g., Corrosion) of a Confined Metal Surface. *Proc. Natl. Acad. Sci. U. S. A.* **2017**, *114* (36), 9541−9546.
(31) Hsiao, Y. H.; La Plante, E. C.; Krishnan, N. M. A.; Dobbs, H. A.; Le Pape, Y.; Neithalath, N.; Bauchy, M.; Israelachvili, J.; Sant, G. Role of Electrochemical Surface Potential and Irradiation on Garnet-Type Almandine's Dissolution Kinetics. *J. Phys. Chem. C* **2018**, *122* (30), 17268−17277.
(32) Walther, J. V. Relation between Rates of Aluminosilicate Mineral Dissolution, PH, Temperature, and Surface Charge. *Am. J. Sci.* **1996**, *296* (7), 693−728.
(33) Carroll-Webb, S. A.; Walther, J. V. A Surface Complex Reaction Model for the PH-Dependence of Corundum and Kaolinite Dissolution Rates. *Geochim. Cosmochim. Acta* **1988**, *52* (11), 2609−2623.
(34) Iler, R. K. *The Chemistry of Silica: Solubility, Polymerization, Colloid and Surface Properties, and Biochemistry*; Wiley: New York, 1979.
(35) Dove, P. M.; Han, N.; Wallace, A. F.; De Yoreo, J. J. Kinetics of Amorphous Silica Dissolution and the Paradox of the Silica Polymorphs. *Proc. Natl. Acad. Sci. U. S. A.* **2008**, *105* (29), 9903−9908.
(36) Tombácz, E.; Szekeres, M. Interfacial Acid-Base Reactions of Aluminum Oxide Dispersed in Aqueous Electrolyte Solutions. 1. Potentiometric Study on the Effect of Impurity and Dissolution of Solid Phase. *Langmuir* **2001**, *17* (5), 1411−1419.
(37) Dove, P. M.; Nix, C. J. The Influence of the Alkaline Earth Cations, Magnesium, Calcium, and Barium on the Dissolution Kinetics of Quartz. *Geochim. Cosmochim. Acta* **1997**, *61* (16), 3329−3340.
(38) Dove, P. M. The Dissolution Kinetics of Quartz in Aqueous Mixed Cation Solutions. *Geochim. Cosmochim. Acta* **1999**, *63* (22), 3715−3727.
(39) Dove, P. M.; Elston, S. F. Dissolution Kinetics of Quartz in Sodium Chloride Solutions: Analysis of Existing Data and a Rate Model for 25°C. *Geochim. Cosmochim. Acta* **1992**, *56* (12), 4147−4156.
(40) La Plante, E. C.; Oey, T.; Hsiao, Y. H.; Perry, L.; Bullard, J. W.; Sant, G. Enhancing Silicate Dissolution Kinetics in Hyperalkaline Environments. *J. Phys. Chem. C* **2019**, *123* (6), 3687−3695.
(41) Chai, L.; Klein, J. Large Area, Molecularly Smooth (0.2 Nm Rms) Gold Films for Surface Forces and Other Studies. *Langmuir* **2007**, *23* (14), 7777−7783.
(42) Valtiner, M.; Kristiansen, K.; Greene, G. W.; Israelachvili, J. N. Effect of Surface Roughness and Electrostatic Surface Potentials on Forces between Dissimilar Surfaces in Aqueous Solution. *Adv. Mater.* **2011**, *23* (20), 2294−2299.
(43) Israelachvili, J.; Min, Y.; Akbulut, M.; Alig, A.; Carver, G.; Greene, W.; Kristiansen, K.; Meyer, E.; Pesika, N.; Rosenberg, K.; Zeng, H. Recent Advances in the Surface Forces Apparatus (SFA) Technique. *Rep. Prog. Phys.* **2010**, *73* (3), 16.
(44) A previous study[28] of electrochemically enhanced dissolution in acidic conditions found an increasing and unbounded exponential relationship between dissolution rate and potential of a gold-coated spherical cap electrode (R = 20 mm) in close proximity to a dissolving silica surface. The contact geometry resulted in a much lower contact area (~80 μm^2) than in the current work (0.7 cm^2), and diffusion path lengths have been shown to influence the dissolution rates of silicates at confined interfaces.[45]
(45) Meyer, E. E.; Greene, G. W.; Alcantar, N. A.; Israelachvili, J. N.; Boles, J. R. Experimental Investigation of the Dissolution of Quartz by a Muscovite Mica Surface: Implications for Pressure Solution. *J. Geophys. Res.* **2006**, *111* (B8), B08202.
(46) Seidel, A.; Lobbus, M.; Vogelsberger, W.; Sonnefeld, J. The Kinetics of Dissolution of Silica "Monospher" into Water at Different Concentrations of Background Electrolyte. *Solid State Ionics* **1997**, *101−103*, 713−719.
(47) Meder, F.; Hintz, H.; Koehler, Y.; Schmidt, M. M.; Treccani, L.; Dringen, R.; Rezwan, K. Adsorption and Orientation of the Physiological Extracellular Peptide Glutathione Disulfide on Surface Functionalized Colloidal Alumina Particles. *J. Am. Chem. Soc.* **2013**, *135* (16), 6307−6316.
(48) Sprycha, R. Electrical Double Layer at Alumina/Electrolyte Interface I. Surface Charge and Zeta Potential. *J. Colloid Interface Sci.* **1989**, *127* (1), 1−11.
(49) Requena, J.; Moreno, R.; Moya, J. S. Alumina and Alumina/Zirconia Multilayer Composites Obtained by Slip Casting. *J. Am. Ceram. Soc.* **1989**, *72* (8), 1511−1513.
(50) Scales, P. J.; Grieser, F.; Healy, T. W.; White, L. R.; Chan, D. Y. C. Electrokinetics of the Silica-Solution Interface: A Flat Plate Streaming Potential Study. *Langmuir* **1992**, *8* (3), 965−974.
(51) Kim, K. M.; Kim, H. M.; Lee, W. J.; Lee, C. W.; Kim, T. Il; Lee, J. K.; Jeong, J.; Paek, S. M.; Oh, J. M. Surface Treatment of Silica Nanoparticles for Stable and Charge-Controlled Colloidal Silica. *Int. J. Nanomed.* **2014**, *9*, 29−40.
(52) Júnior, J. A. A.; Baldo, J. B. The Behavior of Zeta Potential of Silica Suspensions. *New J. Glass Ceram.* **2014**, *4* (2), 29−37.
(53) Schwer, C.; Kenndler, E. Electrophoresis in Fused-Silica Capillaries: The Influence of Organic Solvents on the Electroosmotic Velocity and the Zeta Potential. *Anal. Chem.* **1991**, *63* (17), 1801−1807.
(54) de Lint, W. B. S.; Zivkovic, T.; Benes, N. E.; Bouwmeester, H. J. M.; Blank, D. H. A. Electrolyte Retention of Supported Bi-Layered Nanofiltration Membranes. *J. Membr. Sci.* **2006**, *277* (1−2), 18−27.
(55) Nishimura, S.; Tateyama, H.; Tsunematsu, K.; Jinnai, K. Zeta Potential Measurement of Muscovite Mica Basal Plane-Aqueous Solution Interface by Means of Plane Interface Technique. *J. Colloid Interface Sci.* **1992**, *152* (2), 359−367.
(56) Morga, M.; Adamczyk, Z.; Gödrich, S.; Oćwieja, M.; Papastavrou, G. Monolayers of Poly-l-Lysine on Mica - Electrokinetic Characteristics. *J. Colloid Interface Sci.* **2015**, *456*, 116−124.
(57) Lameiras, F. S.; Souza, A. L. de; Melo, V. A. R. de; Nunes, E. H. M.; Braga, I. D. Measurement of the Zeta Potential of Planar Surfaces with a Rotating Disk. *Mater. Res.* **2008**, *11* (2), 217−219.
(58) Scales, P. J.; Grieser, F.; Healy, T. W. Electrokinetics of the Muscovite Mica-Aqueous Solution Interface. *Langmuir* **1990**, *6* (3), 582−589.
(59) Scales, P. J.; Healy, T. W.; Evans, D. F. The Zeta Potential of Muscovite Mica: Counterion Complexation by a Macrocyclic Ligand. *J. Colloid Interface Sci.* **1988**, *124* (2), 391−395.
(60) Sze, A.; Erickson, D.; Ren, L.; Li, D. Zeta-Potential Measurement Using the Smoluchowski Equation and the Slope of the Current-Time Relationship in Electroosmotic Flow. *J. Colloid Interface Sci.* **2003**, *261* (2), 402−410.
(61) Kumar, B.; Crittenden, S. R. Stern Potential and Debye Length Measurements in Dilute Ionic Solutions with Electrostatic Force Microscopy. *Nanotechnology* **2013**, *24* (43), 435701.

DOI: 10.1021/acs.langmuir.9b02043
Langmuir 2019, 35, 15651−15660

(62) Kirby, B. J.; Hasselbrink, E. F. Zeta Potential of Microfluidic Substrates: 1. Theory, Experimental Techniques, and Effects on Separations. *Electrophoresis* **2004**, *25* (2), 187−202.
(63) Icenhower, J. P.; Dove, P. M. The Dissolution Kinetics of Amorphous Silica into Sodium Chloride Solutions: Effects of Temperature and Ionic Strength. *Geochim. Cosmochim. Acta* **2000**, *64* (24), 4193−4203.
(64) Israelachvili, J. N. *Intermolecular and Surface Forces*, 3rd ed.; Academic Press: 2011.
(65) Hogg, R.; Healy, T. W.; Fuerstenau, D. W. Mutual Coagulation of Colloidal Dispersions. *Trans. Faraday Soc.* **1966**, *62*, 1638−1651.
(66) Chan, D. Y. C.; Healy, T. W.; Supasiti, T.; Usui, S. Electrical Double-Layer Interaction between Oppositely Charged Dissimilar Oxide Surfaces with Charge Regulation and Stern-Grahame Layers. *J. Colloid Interface Sci.* **2006**, *296* (1), 150−158.
(67) Lima, E. R. A.; Boström, M.; Schwierz, N.; Sernelius, B. E.; Tavares, F. W. Attractive Double-Layer Forces between Neutral Hydrophobic and Neutral Hydrophilic Surfaces. *Phys. Rev. E* **2011**, *84*, 061903.
(68) Bell, G. I. Models for the Specific Adhesion of Cells to Cells. *Science* **1978**, *200*, 618−627.

DOI: 10.1021/acs.langmuir.9b02043
Langmuir 2019, 35, 15651−15660

Supporting Information

Electrochemically enhanced dissolution of silica and alumina in alkaline environments

Howard A. Dobbs,[1,‖] George D. Degen,[1,‖] Zachariah J. Berkson,[1,§] Kai Kristiansen,[1] Alex M. Schrader,[1] Tandré Oey,[3] Gaurav Sant,[3,4,5] Bradley F. Chmelka,[1] Jacob N. Israelachvili[1,2]*

[1] Department of Chemical Engineering and [2] Materials Department, University of California, Santa Barbara, California 93106, United States

[3] Department of Civil and Environmental Engineering, [4] Department of Materials Science and Engineering, and [5] California NanoSystems Institute, University of California, Los Angeles, California 90095, United States

S1. Approximation of the average pressure of the contact area

From the Hertz theory of contact mechanics,[1] the average pressure (P) between crossed cylinders of radius R is related to the contact radius (a) and the effective combined modulus (E^*) by the following equation:

$$P = 4aE^*/3\pi R$$

with

$$E^* = E/(1 - \nu^2)$$

where E is the elastic modulus and ν is the Poisson's ratio of the surfaces. Assuming an effective combined elastic modulus E^* of the layered mica-glue-glass composite used in these experiments of approximately 10 GPa, an approximate contact radius (a) of 50 μm, and a radius of curvature (R) of 2 cm, the approximate average pressure is 11 MPa or 110 atm, and the pressure at the center of the contact area is 165 atm.

S2. Approximation of the local pressure at the surface of a confined nanoparticle

With one particle of diameter d between the mica surfaces, the mica is distorted over a lateral distance X from the particle given by:[2]

$$X = [(8dt^3E)/(3P(1-\nu^2))]^{1/4}$$

where t is the thickness of the mica and E is the elastic modulus of the mica. The elastic modulus of the mica rather than the effective modulus of the layered composite is used because the size of the particle is small relative to the mica thickness. A lower bound on the local pressure p between the particle and the mica is given by:

$$p = 4X^2P/d^2$$

Taking d = 200 nm, E = 70 GPa,[3] ν = 0.25,[4] t = 4 μm, and P = 11 MPa the radius of the distortion caused by the nanoparticle is X = 20 μm and the local pressure at the surface of the nanoparticle is p = 500 GPa. The expression underestimates the local pressure, because the contact area between the particle and the mica will be smaller than the projected area of the particle ($\pi d^2/4$). Furthermore, pressure at asperities on the particle will be higher still than the average pressure on the particle.

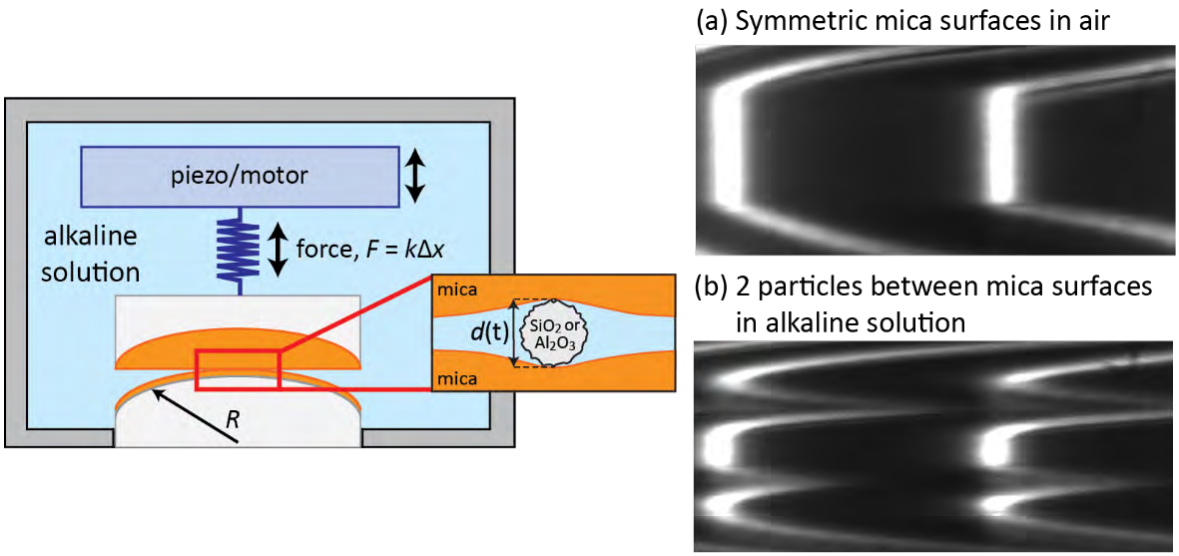

Figure S1. Schematic of SFA experimental setup used to measure the dissolution of silica and alumina nanoparticles trapped between mica surfaces in alkaline solutions. The interference fringes show the surface profile for (a) symmetric mica surfaces in air and (b) a silica or alumina particle confined between the same mica surfaces in an alkaline solution (0.1 mM NaOH, pH 10). The particle diameter (*d*) is calculated from the shift in wavelength of the interference fringes.

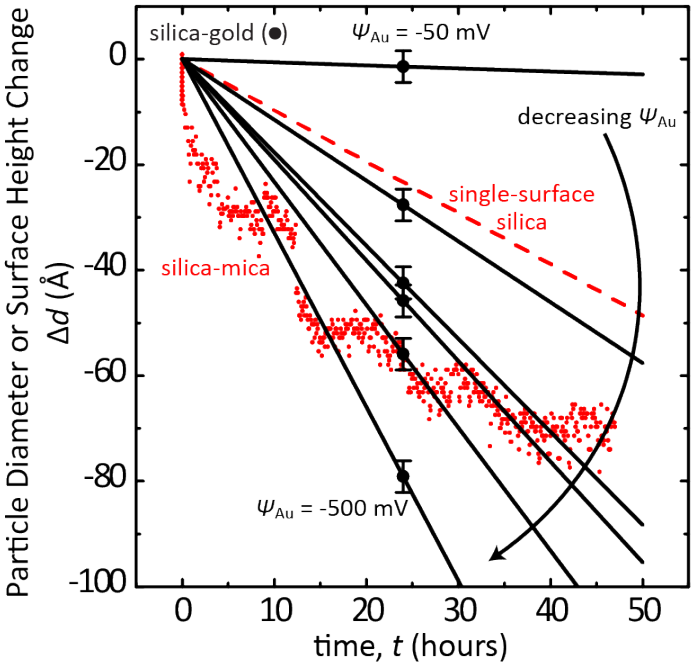

Figure S2. Dissolution of an amorphous silica surface in close proximity to a gold electrode at different applied potentials in an alkaline solution (0.1 mM NaOH, pH 10) (black circles, data from Figure 1 in the main text) compared to dissolution of an amorphous silica nanoparticle in close proximity to mica surfaces at the same solution conditions (red circles, data from Figure 2 in the main text).

S3. Saturation of the volume around a confined dissolving nanoparticle

Following the derivation of Perkin et al.,[2] a particle of diameter d between compressed elastic sheets distorts the sheets, with distortion extending a radial distance X given by:

$$X = [(8dt^3E)/(3P(1 - \nu^2))]^{1/4}$$

The separation between the sheets (y) is given by:

$$y = (3PX^2(1 - \nu^2)/8Et^3)(X^2 - x^4/X^2 + 4r^2\ln(x/X))$$

where x is the radial distance from the particle. Integration yields the volume between the surfaces (V) created by the particle:

$$V = \pi PX^6(1 - \nu^2)/16Et^3 = [(2\pi^2d^3t^3E)/(27P(1 - \nu^2))]^{1/2}$$

Taking d = 200 nm, E = 70 GPa,[3] ν = 0.25,[4] t = 4 μm, and P = 11 MPa (see section S1) yields V = 50 μm^3. The solubility limit of amorphous silica (SiO_2) at pH 10 and T = 25 °C is 310 ppm = 0.31 g/L. If the silica particle (d = 200 nm) dissolves 10 nm, the dissolved volume is 0.005 μm^3, the dissolved mass is 1.05×10^{-5} ng, and the concentration is 2000 g/L, assuming that dissolving species remain in the volume around the particle, well above the solubility limit. To roughly account for diffusion, Fick's law gives:

$$J = -\mathcal{D}(\mathrm{d}c/\mathrm{d}x)$$

where J is the flux per unit area, $\mathcal{D}$ is the diffusion coefficient of the dissolving species, and c is the concentration of the species. Assuming steady state, the rate of material transport of dissolved species through the gap of cross-sectional area A, height h_{gap}, and width w between the mica surfaces outside the volume created by the particle is approximately:

$$JA = (-\mathcal{D}\Delta c/w)(2\pi Xh_{gap})$$

The radius of the contact between the mica surfaces is approximately 50 μm, and the radius of the distortion caused by the particle is approximately X = 20 μm, and therefore w = 30 μm. Assuming atomic contact between the surfaces due to the high pressure (110 atm) gives h_{gap} = 3 Å. Assuming a saturated silica solution gives Δc = 0.31 g/L = 310 g/m^3. The diffusion coefficient[5] of dissolved silica in bulk water at 25 °C is 1×10^{-9} m^2/s. Since the diffusion coefficients of free ions in gaps as narrow as 3 Å have been shown to be within two orders of magnitude of the diffusion coefficients of ions in bulk water,[6] we take this diffusion coefficient as an approximation of the diffusion coefficient for dissolved silica in the gap. These values yield a mass transport rate of 2×10^{-12} g/hr. This rate of mass transport is much less than the rate needed to keep the concentration of dissolved silica in the volume around the particle lower than the solubility limit, supporting the argument that transport limitations slow dissolution of confined particles.

References

(1) Johnson, K. L. *Contact Mechanics*; Cambridge University Press: Cambridge, 1985.

(2) Perkin, S.; Chai, L.; Kampf, N.; Raviv, U.; Briscoe, W.; Dunlop, I.; Titmuss, S.; Seo, M.; Kumacheva, E.; Klein, J. Forces between Mica Surfaces, Prepared in Different Ways, Across Aqueous and Nonaqueous Liquids Confined to Molecularly Thin Films. *Langmuir* **2006**, *22*, 6142–6152.

(3) Zhang, G.; Wei, Z.; Ferrell, R. E.; Guggenheim, S.; Cygan, R. T.; Luo, J. Evaluation of the Elasticity Normal to the Basal Plane of Non-Expandable 2:1 Phyllosilicate Minerals by Nanoindentation. *Am. Mineral.* **2010**, *95* (5–6), 863–869.

(4) Christensen, N. I. Poisson's Ratio and Crustal Seismology. *J. Geophys. Res.* **1996**, *101* (B2), 3139–3156.

(5) Rebreanu, L.; Vanderborght, J. P.; Chou, L. The Diffusion Coefficient of Dissolved Silica Revisited. *Mar. Chem.* **2008**, *112* (3–4), 230–233.

(6) Alcantar, N.; Israelachvili, J.; Boles, J. Forces and Ionic Transport between Mica Surfaces: Implications for Pressure Solution. *Geochim. Cosmochim. Acta* **2003**, *67* (7), 1289–1304.